



Original Research Paper

Growth mechanism and photocatalytic properties of SrWO₄ microcrystals synthesized by injection of ions into a hot aqueous solutionL.S. Cavalcante^{a,b,*}, J.C. Sczancoski^a, N.C. Batista^b, E. Longo^a, J.A. Varela^a, M.O. Orlandi^a^a LIEC-IQ-Universidade Estadual Paulista, P.O. Box 355, 14801-907 Araraquara, SP, Brazil^b UESPI, CCN, Departamento de Química, Rua João Cabral, P.O. Box 2231, 64002-150 Teresina, PI, Brazil

ARTICLE INFO

Article history:

Received 23 February 2012

Received in revised form 7 June 2012

Accepted 8 August 2012

Available online 11 September 2012

Keywords:

SrWO₄

Rhodamine

Rietveld refinement

Hot-injection

Photocatalysis

ABSTRACT

This paper reports our initial research to obtain SrWO₄ microcrystals by the injection of ions into a hot aqueous solution and their photocatalytic (PC) properties. These microcrystals were structurally characterized by X-ray diffraction (XRD), Rietveld refinements and Fourier transform (FT)-Raman spectroscopy. The shape and average size of these SrWO₄ microcrystals were observed by field emission scanning electron microscopy (FE-SEM) and transmission electron microscopy (TEM). In addition, we have investigated the PC activity of microcrystals for the degradation of rhodamine B (RhB) and rhodamine 6G (Rh6G) dyes. XRD patterns, Rietveld refinement data and FT-Raman spectroscopy confirmed that SrWO₄ microcrystals have a scheelite-type tetragonal structure without deleterious phases. FT-Raman spectra exhibited 12 Raman-active modes in a range from 50 to 1000 cm⁻¹. FE-SEM and TEM images suggested that the SrWO₄ microcrystals (rice-like – 95%; star-, flower-, and urchin-like – 5%) were formed by means of primary/secondary nucleation events and self-assembly processes. Based on these FE-SEM/TEM images, a crystal growth mechanism was proposed and discussed in details in this work. Finally, a good PC activity was first discovered of the SrWO₄ microcrystals for the degradation of RhB after 80 min and Rh6G after 50 min dyes under ultraviolet-light, respectively.

© 2012 The Society of Powder Technology Japan. Published by Elsevier B.V. and The Society of Powder Technology Japan. All rights reserved.

1. Introduction

Commonly, the strontium tungstate (SrWO₄) crystals have been prepared by oxide mixture or solid state reaction [1–3], Czochralski [4–6] and double decomposition flux [7]. However, these techniques use high heat treatment temperatures, long processing times and/or complex equipments. In order to minimize these drawbacks, other synthetic routes were developed over the years to obtain the SrWO₄ crystals at micro-, meso- and nanoscale [8–11], for example: co-precipitation [12,13], electrochemical [14,15], biomimetic system of a supported liquid membrane [16], sonochemical [17], conventional hydrothermal [18], solvothermal [19–21], microwave-hydrothermal [22] and cyclic-microwave [23]. The positive point of these methods is ability of forming crystals with different sizes, shapes and structures [24,25]. In particular, the conventional hydrothermal system has been widely used in the preparation of tungstates with distinct morphological aspects [26]. However, this chemical route presents a low kinetics of formation and crystallization of materials, resulting in long processing times (in the range from 12 h to 48 h) [27].

In particular, the tungstates (AWO₄, A = Ca, Sr, Ba and Pb) with a scheelite-type tetragonal structure exhibit an excellent photoluminescence (PL) property at room temperature [28–31]. However, few studies on the photocatalytic (PC) activity have been reported in the literature [32–34].

Therefore, this paper reports our initial research on the synthesis of SrWO₄ microcrystals by the injection of ions into a hot aqueous solution (IIHAS) method. The structural refinement, growth mechanism, and PC activity for the degradation of rhodamine B (RhB) and rhodamine 6G (Rh6G) were discussed in details.

2. Experimental procedure

2.1. Synthesis of SrWO₄ microcrystals

SrWO₄ microcrystals were prepared by the hot-injection technique. The typical experimental procedure is described as follows: 1 × 10⁻³ mol of sodium tungstate (VI) dihydrate (Na₂WO₄·2H₂O) (99.5% purity, Sigma–Aldrich) and 1 × 10⁻³ mol of strontium (II) nitrate [Sr(NO₃)₂] (99% purity, Sigma–Aldrich) were separately dissolved in two plastic tubes (Falcon) with 50 mL of deionized water. The first solution with Na⁺ and WO₄²⁻ ions was transferred to a 250 mL glass flask (Boeco-boro 3.3, Germany) and heated up to 90 °C under constant stirring for 10 min. Then, the second solution containing the Sr²⁺ and NO₃⁻ ions was sucked by a syringe and

* Corresponding author at: LIEC-IQ-Universidade Estadual Paulista, P.O. Box 355, 14801-907 Araraquara, SP, Brazil. Tel.: +55 16 3361 5215; fax: +55 16 3361 8214.
E-mail address: laeiosc@bol.com.br (L.S. Cavalcante).

Table 1

Lattice parameters, unit cell volume, atomic coordinates and site occupation obtained by the Rietveld refinement of SrWO₄ microcrystals.

Atoms	Wyckoff	Site	S.O.F	x	y	z
Strontium	4b	−4	1	0	0.25	0.625
Tungsten	4a	−4	1	0	0.25	0.125
Oxygen	16f	1	1	0.27454	0.09845	0.04842

$a = b = 5.4226 \text{ \AA}$; $c = 11.9214 \text{ \AA}$; $V = 350.54 \text{ \AA}^3$; $R_w = 9.8\%$; $R_{wmb} = 9.58\%$; $R_b = 6.0\%$; $R_{exp} = 2.8\%$ and $\sigma = 3.5$.

S.O.F = Site occupancy factor; SrWO₄ microcrystals obtained by injection of ions into a hot aqueous solution (90 °C); *CIFs generated from Rietveld refinements in Supplementary data.

the rapid formation and crystallization caused by the fast injection of Sr²⁺ ions into hot aqueous solutions that contain the WO₄^{2−} ions.

3.2. Representation of the SrWO₄ unit cells

Fig. 2 illustrates a schematic representation for the SrWO₄ tetragonal structure modeled by means of Rietveld refinement data.

This structure was modeled through the Visualization for Electronic and Structural Analysis (VESTA) program version 3.0.7 for Windows [42], using the lattice parameters and atomic positions obtained from Rietveld refinement shown in Table 1. The SrWO₄ crystals belong to scheelite-type tetragonal structure with space group (*I*4₁/*a*), point-group symmetry (*C*_{4h}⁶) and four molecules per unit cell (*Z* = 4) [43]. Fig. 2 shows that the bonds between O–W–O and O–Sr–O atoms were projected out of the unit cell. In these tetragonal structures, tungsten (W) atoms are coordinated to four oxygen atoms, which form [WO₄] clusters with a tetrahedral configuration, a symmetry group (*T*_d) and tetrahedrons polyhedra (4 vertices, 4 faces and 6 edges) [44]. These [WO₄] clusters are slightly distorted into the lattice in all SrWO₄ crystals. The differences in the (O–W–O) bond angles can lead to the different levels of order–disorder and/or distortions into the lattice. In addition, in this structures, the strontium (Sr) atoms are bonded to eight oxygen atoms, resulting in [SrO₈] clusters with deltahedral configuration, symmetry group (*D*_{2d}) and snub–dispenoide polyhedra (8 vertices, 12 faces and 18 edges) [45]. Moreover, we note possible distortions on the [SrO₈] clusters due to the different bond angles between

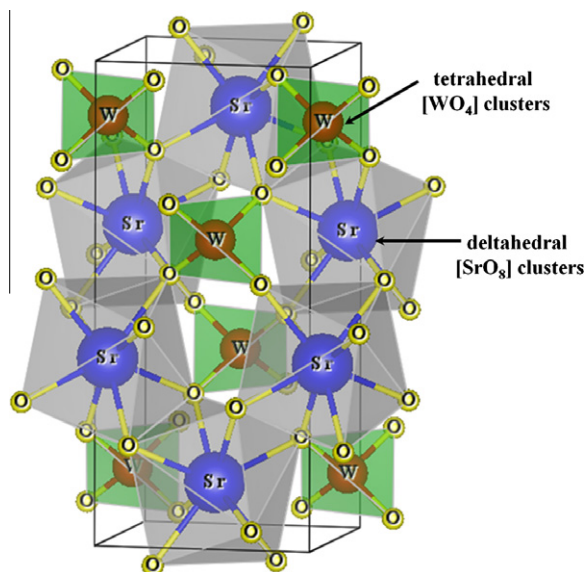


Fig. 2. Schematic representation of SrWO₄ tetragonal structure.

O–Sr–O. However, this situation is more complicated and it is necessary to be more analyzed and explained with details in a future work.

3.3. FT-Raman spectroscopy analysis

The group theory calculations confirm that the tungstates with scheelite-type tetragonal structure exhibit 26 different (Raman and infrared) vibrational modes, as represented by the Eq. (4) [46]:

$$\Gamma_{(\text{Raman+Infrared})} = 3A_g + 5A_u + 5B_g + 3B_u + 5E_g + 5E_u \quad (4)$$

where A_g , B_g , and E_g are Raman-active modes, A and B modes are nondegenerate and E modes are doubly degenerate. The subscripts “g” and “u” indicate the parity under inversion in centrosymmetric SrWO₄ crystals. A_u and E_u modes correspond to acoustic mode zero frequency while the others are optic modes. In addition, the A_g , B_g and E_g modes arise from the same motion in a SrWO₄ phase. Thus, we expect that there are 13 zone-center Raman-active modes for SrWO₄ crystals as described in Eq. (5) [46]:

$$\Gamma_{(\text{Raman})} = 3A_g + 5B_g + 5E_g \quad (5)$$

According to the literature [47], vibrational modes detected in tungstate Raman spectra can be classified into two groups: external and internal modes. Vibrational external modes are related to the lattice phonon or motion of [SrO₈] clusters, and vibrational internal modes are caused by the vibration of [WO₄] clusters (the mass center is in the stationary state). An isolated [WO₄] cluster has a cubic symmetry point (*T*_d) [48], and its vibrations are composed of four modes [$\nu_1(A_1)$, $\nu_2(E_1)$, $\nu_3(F_2)$ and $\nu_4(F_2)$], one free rotation mode $\nu_{r.}(F_1)$ and one translational mode (F_2). On the other hand, when [WO₄] clusters are located in the scheelite structure, its point symmetry is reduced to *S*₄ [49].

Fig. 3 shows the FT-Raman spectrum of SrWO₄ microcrystals obtained by the ITHAS method at 90 °C.

This figure indicates that only 12 Raman-active vibrational modes were detected experimentally. According to the literature [50], Raman spectra provide information on the degree of structural order–disorder at short-range in ABO₄ materials. The sharp and intense Raman-active modes indicate that the SrWO₄ crystals are structurally ordered at short-range with a strong interaction between clusters because of the symmetric stretching (←O–W→O→) (see inset in Fig. 3). The positions of each Raman

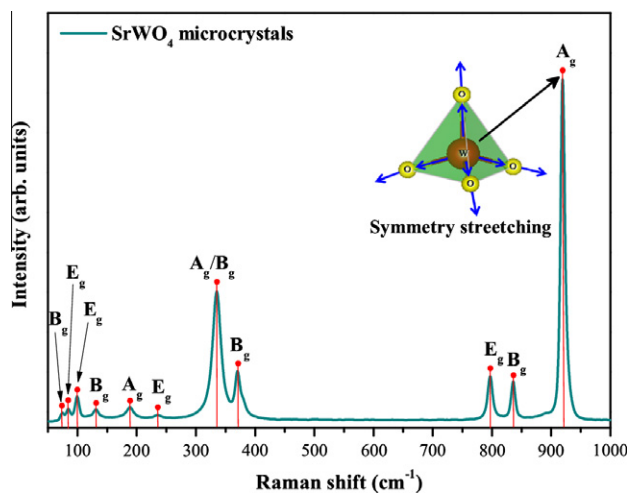


Fig. 3. FT-Raman spectrum of SrWO₄ microcrystals. The vertical lines indicate the positions and relative intensities of Raman-active modes. Inset shows the symmetric stretching of (←O–W→O→) bonds.

Table 2Comparative results between the experimental Raman-active modes of SrWO₄ microcrystals obtained in this work with those reported in the literature.

M	T (°C)	t (min)	B _g	E _g	E _g	B _g	A _g	E _g	A _g	B _g	B _g	E _g	B _g	A _g	Ref.
CZ	1200	2880	78	–	101	131	187	238	334	334	370	797	839	925	[51]
CMI	–	20	–	–	–	–	–	190	–	337	372	794	838	922	[52]
CZ	1300	1440	75	–	102	133	190	238	336	336	374	800	837	921	[53]
CMI	–	20	–	–	–	–	190	–	–	337	372	799	838	922	[54]
IHAS	90	10	73	82	99	131	189	235	336	336	371	797	837	920	×

M = method; T = temperature; t = time; Raman modes = (cm⁻¹); CZ = Czochralski; CZ = Czochralski; CMI = cyclic microwave radiation; IHAS = injection of ions into a hot aqueous solution and × = this work.

vibrational mode found in this work were compared with those reported in the literature [51–54] (Table 2).

The results reported in this table indicate that all Raman-active modes of SrWO₄ crystals prepared by the IHAS method are arising from the scheelite-type tetragonal structure [51–54]. This table reveals that some relative positions of Raman modes have small shifts, which can be caused by several factors, such as: preparation method, average particle size, distortions on the (O–W–O)/(O–Sr–O) bonds, interaction forces between [WO₄]-[SrO₈]-[WO₄] clusters and/or different degrees of structural order–disorder at short-range. Also, the relative positions for the free rotation $\nu_{fr}(F_1)$ modes of SrWO₄ crystals demonstrate a slightly shift. This behavior can be associated to the distortions on the [SrO₈] clusters as a consequence of the synthesis method employed in this work.

3.4. FE-SEM analysis

Fig. 4a–e shows the FE-SEM images of SrWO₄ microcrystals.

The FE-SEM image in Fig. 4a illustrates several rice-like SrWO₄ microcrystals with agglomerate nature, exhibiting quasi-monodisperse sizes and shapes. This image indicates that these microcrystals are rapidly formed after the injection of ions, promoting a fast precipitation reaction [55]

FE-SEM image clearly show four types of superstructures: rice-, star-, flower- and urchin-like SrWO₄ microcrystals (Fig. 4a–e), respectively. Fig. 4a and b reveal a high percentage (~95%) of rice-like SrWO₄ microcrystals. The star-like SrWO₄ microcrystals exhibit an average size distribution in the range from 13.6 μm to 15 μm. In this system, it is estimated that these superstructures have an average size of approximately 14.2 μm. Fig. 4c displays a star-like SrWO₄ microcrystal formed by two rice-like SrWO₄ microcrystals. These four elongated extremities can be divided to form new tips, also it is possible that other two crystals can aggregate to growth of the flower-like SrWO₄ microcrystals (Fig. 4d). Finally, these flowers-like crystals grow to form urchin-like SrWO₄ microcrystals (Fig. 4e).

3.5. TEM, HR-TEM and SAED analyses

Fig. 5a–h illustrates the TEM/HR-TEM images and SAED patterns of SrWO₄ microcrystals.

Fig. 5a shows a low magnification TEM image of a single rice-like SrWO₄ microcrystal. In principle, the dark contrast in the TEM measurements suggests that these types of crystals are completely rigid and dense. When the HR-TEM was performed on the tip of the microcrystal (rectangle in Fig. 5a), it was evidenced an interplanar distance of approximately 3.2 Å, corresponding to (112) plane (Fig. 5b). The SAED pattern along the [482] zone axis exhibit isolated spots, where its distances denote a typical pattern of scheelite structure (inset in Fig. 5b). Fig. 5c illustrates a low magnification TEM micrograph of a single star-like microcrystal. In this same crystal, it was also performed the HR-TEM image and SAED patterns, as shown in Fig. 5d. The HR-TEM image revealed an interplanar distance of 2.7 Å, related to (200) plane. Analogous to the

previous case, the SAED performed in the [0 $\bar{6}$ 1] zone axis also presented a spot pattern of materials belonging to the scheelite class (inset in Fig. 5d). The flower-like SrWO₄ microcrystals were verified in the TEM images displayed in Fig. 5e. This crystal grew with six tips, but it is possible to find similar crystals with up to eight tips (see Supplementary data-S1). The rectangle in Fig. 5f denotes the specific region where the HR-TEM and SAED were carried out. These images proved that this crystal shape has the same interplanar distance and orientation from those rice-like microcrystals. Therefore, we conclude that these crystals present a typical growth along the [100] direction (see Supplementary data-S2a and b). On the other hand, the crystals with several tips were called of urchin-like shapes (Fig. 5g), where the HR-TEM made on one of its tips (red rectangle in Fig. 5g) allowed to estimate an interplanar distance of 3.2 Å (Fig. 5h), in excellent agreement with the (112) plane. The SAED pattern take from the [1 $\bar{1}$ 0] zone was sufficient to confirm an array of bright spots, commonly noted in monocystals with tetragonal structure.

3.6. Growth mechanism of SrWO₄ microcrystals

Fig. 6a–f shows a schematic representation of all stages involved in the synthesis and growth of SrWO₄ microcrystals synthesized by the injection of ions into a hot aqueous solution.

Fig. 6a illustrates an aqueous solution heated at 90 °C containing WO₄²⁻ ions. In the sequence, Sr²⁺ ions were rapidly injected into this solution with purpose of controlling the kinetics of nucleation and growth of SrWO₄ microcrystals. Consequently, this experimental procedure promoted the formation of a white suspension. As it can be seen in some TEM micrographs, there is a few amount of SrWO₄ nanocrystals, which can be assigned to the SrWO₄ nuclei (Fig. 6b; Supplementary data-S3). In the next growth stage, the self-assembly process predominates between these nanocrystals because of its high surface energies. Also, it is possible to observe the rice-like microcrystals (Fig. 6c) and also the presence of some intermediate SrWO₄ microcrystals (Supplementary data-S4). The XRD patterns and HR-TEM micrographs indicated that these rice-like SrWO₄ microcrystals have a preferential growth along the [100] direction than in the [001] (Supplementary data-S2b). Moreover, these intermediate SrWO₄ microcrystals were able to grow in the star-like shape (Fig. 6d). According to the progressive evolution of these microcrystals, the number of tips was increasing with the growth of these intermediary microcrystals, so that they were referred as flower- and urchin-like shapes, respectively (Fig. 6e and f)

3.7. Photocatalytic activity of SrWO₄ microcrystals for the degradation of RhB and Rh6G dyes

Fig. 7a and b shows the progress in the PC degradation of RhB and Rh6G dyes under UV illumination, where the SrWO₄ microcrystals were employed as catalysts. In the spectra were monitored the maximum absorption bands of these dyes in aqueous solutions. Insets illustrate the digital photos of the RhB and Rh6G up to the

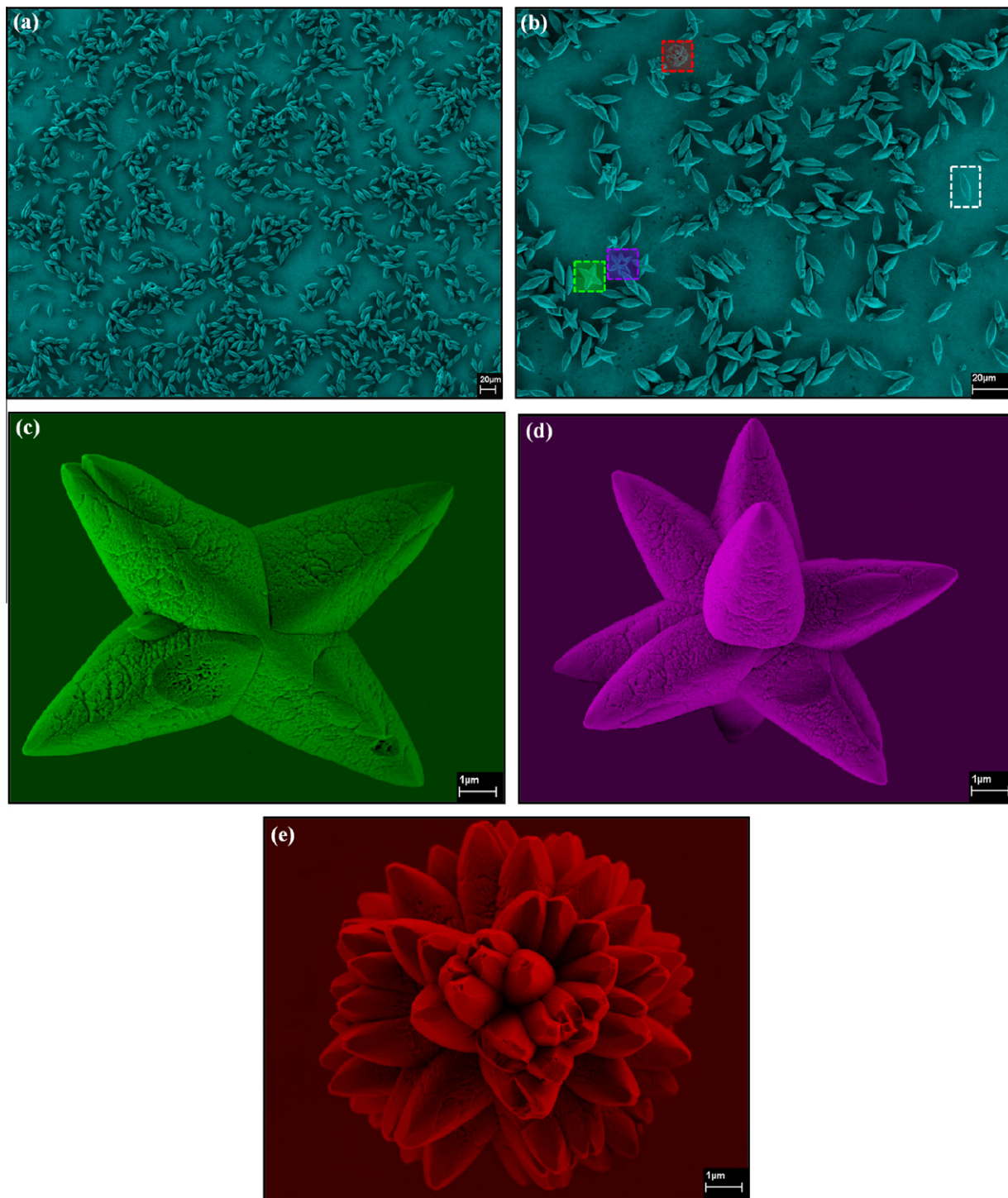


Fig. 4. (a and b) Low magnification FE-SEM images of rice-like SrWO_4 microcrystals, (c) high magnification FE-SEM images of star-like SrWO_4 microcrystals, (d) high magnification FE-SEM images of flower-like SrWO_4 microcrystals and (e) high magnification FE-SEM images of urchin-like SrWO_4 microcrystals.

complete degradation. The degradation rates (C_n/C_0) of both the RhB and Rh6G dyes with and without the catalyst is shown in Fig. 7c and d, and its first-order rate constants (k) are illustrated in Fig. 7e and f.

Fig. 7a reveals a significant reduction in the maximum absorption spectra of RhB during the photodegradation process. Before irradiation, the (N,N,N,N' -tetraethylated rhodamine molecule) RhB dye has one band with the maximum absorption centered at 554 nm. The photodecoloration of RhB dye occurs due to an oxidative attack by one of the active oxygen species on the N -ethyl group

[56]. No displacement in the maximum absorption was verified in the spectra, suggesting that there is not the formation of secondary products during the photodegradation process, such as: N,N,N' -triethylated rhodamine ($\lambda = 539$ nm), N,N' -diethylated rhodamine ($\lambda = 522$ nm), N -ethylated rhodamine ($\lambda = 510$ nm) and rhodamine ($\lambda_{\text{max}} = 498$ nm) [57]. Therefore, we believe that a high percentage of RhB was destroyed or photodegraded after 60 min under UV light illumination (see insets in Fig. 5a). The results indicate that the SrWO_4 has a high efficiency for the degradation of RhB in relation to other scheelites, for example: PbMoO_4 , SrMoO_4 , SrWO_4 ,

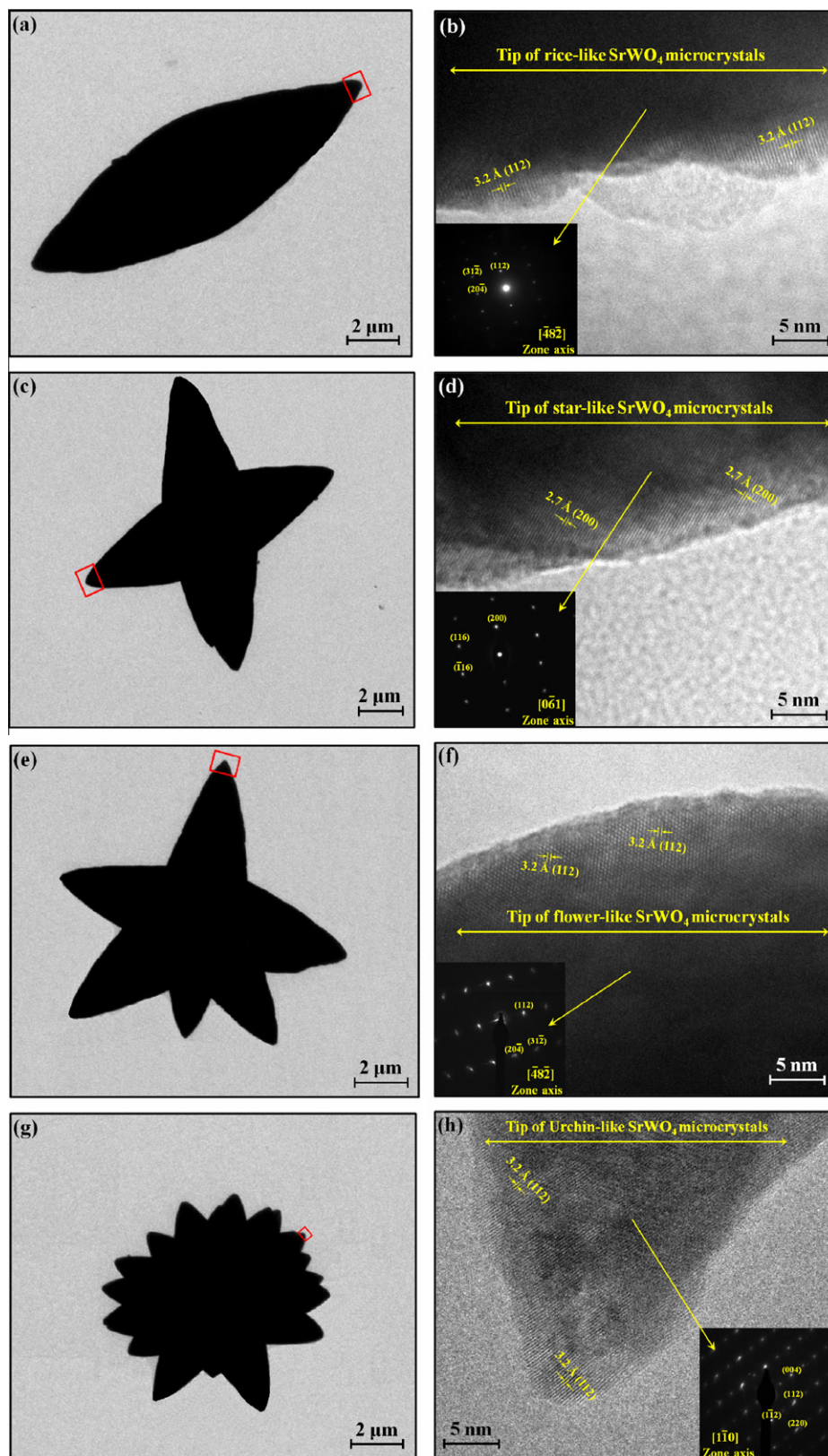


Fig. 5. (a) Low magnification TEM images of rice-like SrWO_4 microcrystals, (b) HR-TEM image and SAED patterns on the tip of rice-like SrWO_4 microcrystals (inset), (c) low magnification TEM images of star-like SrWO_4 microcrystals, (d) HR-TEM image and SAED patterns on the tip of star-like SrWO_4 microcrystals (inset), (e) low magnification TEM images of flower-like SrWO_4 microcrystals, (f) HR-TEM image and SAED patterns on the tip of flower-like SrWO_4 microcrystals (inset), (g) low magnification TEM images of urchin-like SrWO_4 microcrystals and (h) HR-TEM image and SAED patterns on the tip of urchin-like SrWO_4 microcrystals (inset).

CdMoO_4 , PbWO_4 , and CdWO_4 [58,59,32,60–62]. Moreover, the SrWO_4 catalysts presented also a significant response for the degradation of Rh6G (maximum absorption band centered at

526 nm) as a function of UV radiation time (Fig. 5b). We believe that the SrWO_4 crystals present a better capability of acting on the active sites of Rh6G than those of RhB. According to the litera-

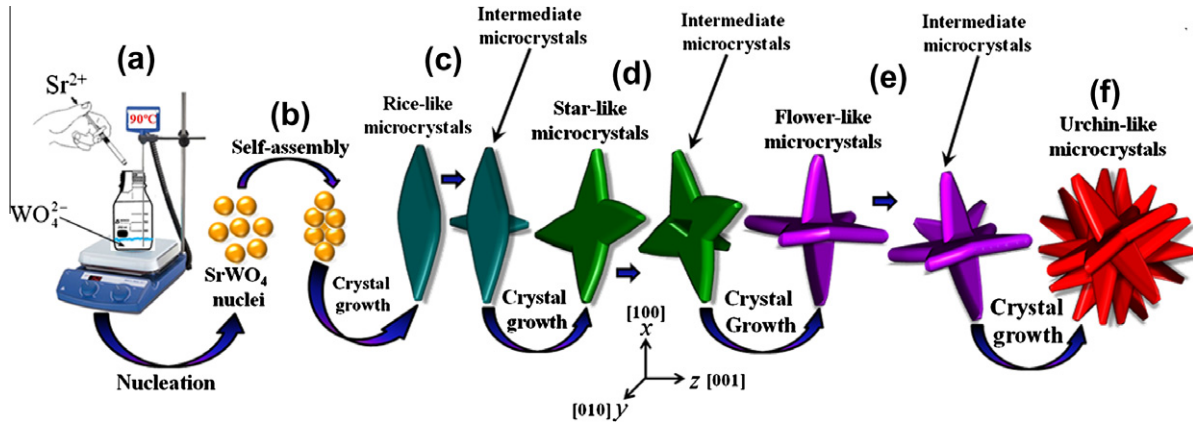
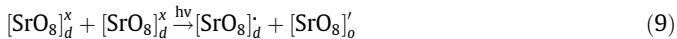
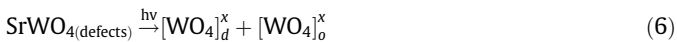


Fig. 6. Schematic representation of the growth mechanism for the SrWO₄ crystals obtained by the IHAS method: (a) nucleation, formation of SrWO₄ nuclei and self-assembly process (b); crystal growth of rice-like SrWO₄ microcrystals (c); crystal growth of star-like SrWO₄ microcrystals (d); crystal growth of flower-like SrWO₄ microcrystals (e); crystal growth of urchin-like SrWO₄ microcrystals (e).

ture [63], the low recombination rate between photogenerated electrons and holes on the crystal surface is the key factor for a good photocatalytic property. Thus, the holes (*h*[•]) generated by the distorted [SrO₈] and [WO₄] clusters can provide favorable conditions for the electron (*e*[•])–hole (*h*[•]) recombination events.

In this work, a model based on complex clusters was proposed to explain the photocatalytic activity of SrWO₄ microcrystals due to the photo-oxidation of RhB and Rh6G. Initially, we assume that before the UV excitation light excitation reaches the system, the SrWO₄ catalyst has the ability to generate *e*[•]–*h*[•] pairs. This phenomenon is caused by the existence of distorted [WO₄]_d/[SrO₈]_d clusters (intrinsic defects) into the scheelite-type tetragonal structure. These defects are able to polarize the lattice and lead to the electronic transitions between [WO₄]_d^x/[SrO₈]_d^x (disordered clusters) and [WO₄]_o^x/[SrO₈]_o^x (ordered clusters). When the UV light is absorbed by the crystals, the following processes can occur:



where [WO₄]_d are distorted clusters located as intermediary energy levels near the valence band (VB) and [WO₄]_o are ordered clusters situated as intermediate energy levels below the conduction band (CB).

In addition, the RhB or Rh6G dye is also excited by the UV light, as shown in the Eqs. (10) and (11):



In the sequence, the UV light ($\lambda = 254 \text{ nm} \approx 4.88 \text{ eV}$) promotes the excitation of several electrons from VB to CB, leading to electronic transference within the band gap (Supplementary data Fig. S5). During the photo-oxidation processes, the species generated as [WO₄]_d and [SrO₈]_d clusters interact with the dyes and water (H₂O) molecules, as indicated in the Eqs. (12)–(17)



On the other hand, the [WO₄]_d/[SrO₈]_d clusters have the tendency of reacting with the H[•] to form the H while the ordered [WO₄]_o' and [SrO₈]_o' clusters interact with the oxygen (O₂) molecules in the aqueous solution, as indicated in the Eqs. (18) and (19):



These cycles continuously occur when the system is exposed to the UV light. Finally, after several cycles of photo-oxidation, the degradation of RhB or Rh6G dye by the formed oxidant species can be expressed by the Eqs. (20) and (21):

After the UV-illumination:



where CCO = colorless compounds organic.

Based on our photocatalytic mechanisms, we assume that the defects on the crystal surface and electronic structure of distorted [WO₄]_d/[SrO₈]_d and ordered [WO₄]_o'/[SrO₈]_o' clusters play an important role in the producing of OH[•] and O₂' radicals, which are the main oxidizing species for the degradation of RhB and Rh6G dyes in aqueous solution.

Fig. 7c and d shows that after 80 min and 50 min under UV-illumination, the RhB and Rh6G were completely degraded, respectively. Based on the results obtained by the kinetic of weight-based (C_n/C₀) photocatalytic degradation of Rh6G and RhB, it was noted that the SrWO₄ crystals have a elevated percentage for the degradation of RhB and Rh6G dyes after 40 min under UV-illumination.

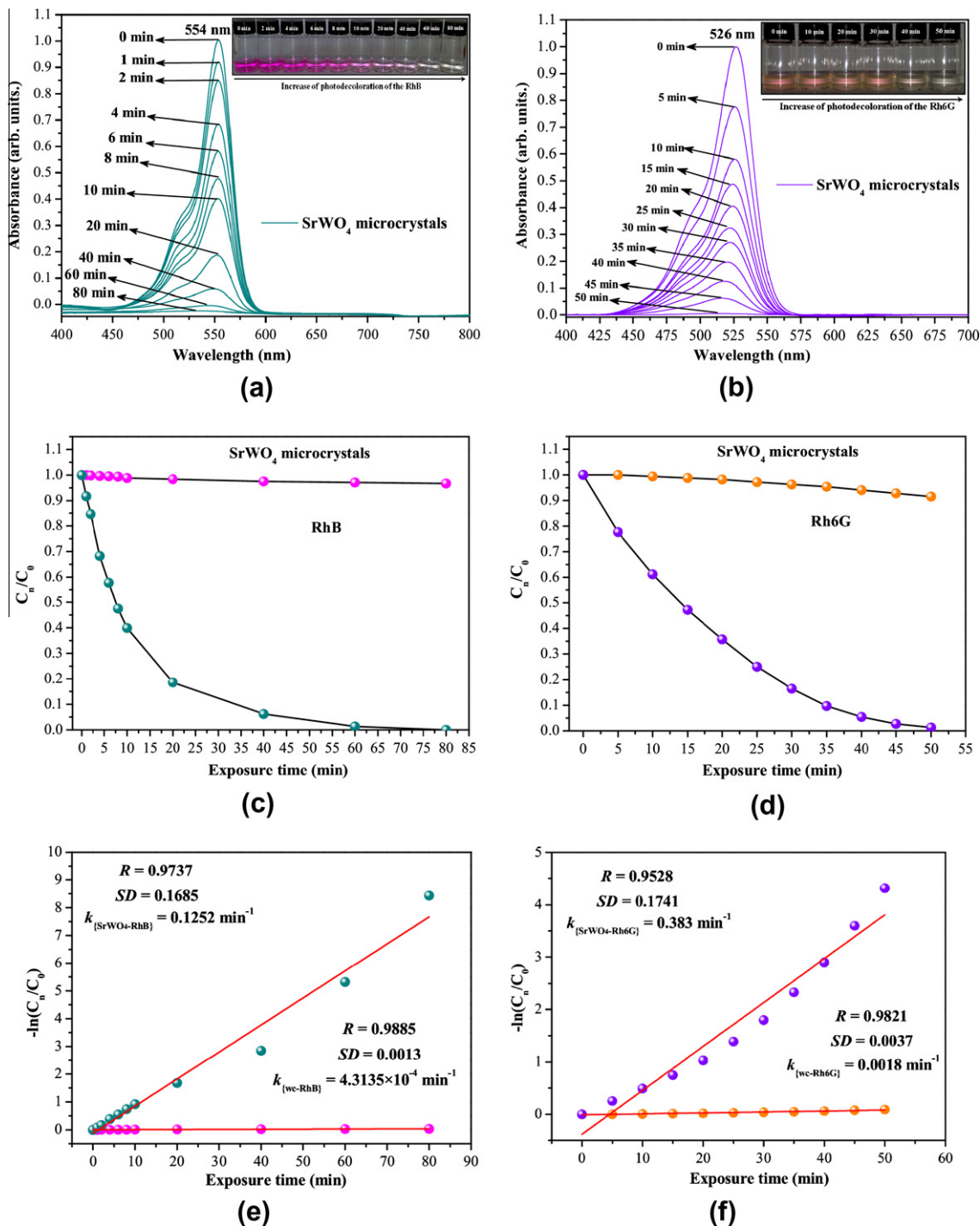


Fig. 7. (a and b) Evolution of UV-vis absorption spectra after 80 min 50 min of illumination for the photodegradation of RhB and Rh6G dyes by the SrWO₄ microcrystals. Inset shows digital photos of photodegradation for the RhB after different illumination times with the UV-lamps, (c and d) kinetic of weight-based photocatalytic degradation of RhB and Rh6G dye by the catalysts and (e and f) first-order kinetic without and with catalysts.

The photocatalytic test was performed to prove the efficiency of our microcrystals as photocatalysts for future industrial applications, especially in the control and treatment of polluted or contaminated waters. Thus, we employ the pseudo-first order rate constants (k) [64] to quantitatively understand the reaction kinetics for the degradation of RhB and Rh6G by the catalyst crystals (Fig. 7e and f), as expressed by the following equation:

$$-\ln\left(\frac{C_n}{C_0}\right) = kt \quad (22)$$

where C_0 is the concentration initial (0 min) of RhB in aqueous solution and C_n is the concentration of RhB in aqueous solution for different times (n (min) = 1, 2, 5, 10, ...) under UV-illumination, t is the time and k is the pseudo-first order constant rate, respectively. Generally, this equation is used for the photocatalytic degradation processes with the initial pollutant concentration lower than 1×10^{-5} mol/L [65]. According to the Eq. (22), if $[-\ln(C_n/C_0)]$ is plotted as a function of t , a straight line should be obtained whose slope is k (min^{-1}). All results shown in Fig. 7e and f are absolute and they were not normalized by the specific surface area (S_{BET}) of the crys-

tals. Fig. 7e and f indicates that the rate constants ($k_{\text{wc-RhB}} = 4.3135 \times 10^{-4}$ and $k_{\text{wc-Rh6G}} = 0.0018 \text{ min}^{-1}$) without catalyst for the degradation of RhB and Rh6G are very small, revealing that both the dyes practically do not degrade after 80 min and 50 min under UV-illumination, respectively. The rate constant values ($k_{[\text{SrWO}_4\text{-RhB}]} = 0.1252$ and $k_{[\text{SrWO}_4\text{-Rh6G}]} = 0.383 \text{ min}^{-1}$) of SrWO_4 microcrystals for the degradation of RhB and Rh6G solutions are displayed in these figures. The obtained results for the correlation coefficient (R) and standard deviation (SD) showed good statistics values of our SrWO_4 crystals and also a elevated rate of degradation RhB and Rh6G in a short time (up to 40 min). SrWO_4 microcrystals produced the following normalized values: $k_{[\text{SrWO}_4\text{-RhB}]} = 0.02966$ and $k_{[\text{SrWO}_4\text{-Rh6G}]} = 0.09075 \text{ min}^{-1}$. The results found after the normalization of the kinetic parameters ($k_{\{\text{absolute}\}}$ and $k_{[\text{normalized}]}$) for the degradation reactions of RhB and Rh6G as well as the S_{BET} values are listed in Table 3. This table shows that the $k_{[\text{normalized}]}$ values are smaller than those of $k_{\{\text{absolute}\}}$, i.e., each catalyst crystal has a specific surface area (S_{BET}).

Therefore, it is necessary to normalize the $k_{\{\text{absolute}\}}$ values. These ($k_{[\text{normalized}]}$) values were estimated dividing the ($k_{\{\text{absolute}\}}$) by the specific area surface (S_{BET}) of each catalyst. After normalization, the rate constants of the catalyst crystals obey the following order: $k_{[\text{SrWO}_4\text{-Rh6G}]} > k_{[\text{SrWO}_4\text{-RhB}]}$. Moreover, after comparing the relationships between $k_{[\text{Rh6G}]} / k_{[\text{RhB}]}$ for the SrWO_4 catalysts, we find that the normalized $k_{[\text{Rh6G}]}$ is approximately 3.06 times higher than the normalized $k_{[\text{RhB}]}$.

In our photocatalytic tests, the initial stage is extremely important for the optimization of the heterogeneous photocatalysis, which is a versatile technique for the degradation of organic pollutants. In this process, before UV-light reaches the liquid phase containing the RhB or Rh6G dye with the SrWO_4 crystals, it is necessary to obtain an optimized dispersion of this system. Therefore, 50 mg of our catalyst crystals were added to the $1 \times 10^{-5} \text{ mol/L}$ of RhB or Rh6G aqueous solutions, which were well dispersed through an ultrasonic process for 10 min. We presume that this step has a fundamental importance for the reproducibility of these results and that the system reaches a perfect adsorption-desorption equilibrium. In the second state, this well-dispersed system was stirred for 5 min inside a dark box and the first aliquot was collected. Then, six UV lights were switch onto start the photocatalysis tests. During all stages, the RhB or Rh6G solution was kept at 20°C by means of a thermostatic bath. After the UV illumination of this system, the excitation of SrWO_4 crystals takes place, and the RhB or Rh6G molecules are adsorbed on the crystal surfaces. As it was noted in the previous analyses, the SrWO_4 crystals have several structural defects and different orientations when compared to those prepared by the conventional standards. These structural characteristics can directly affect the photocatalytic properties of crystals prepared by the ITHAS method at 90°C . Also, we believe that each of the structural defects found on the crystal surfaces can act as active sites for the degradation of RhB or Rh6G, which is in perfect agreement with the recent researches reported in the literature [66,67].

Table 3

Absolute kinetic constants ($k_{\{\}}$), normalized kinetic constants ($k_{[\]}$) and specific area surface (S_{BET}) for the different catalyst crystals.

Samples	$k_{\{\}}$ (min^{-1})	S_{BET} (m^2/g)	$k_{[\]}$ ($\text{min}^{-1}/\text{m}^2 \text{ g}^{-1}$)
wc-RhB	4.3135×10^{-4}	–	–
wc-R6G	0.0018	–	–
$\text{SrWO}_4\text{-RhB}$	0.1252	4.22	0.02966
$\text{SrWO}_4\text{-Rh6G}$	0.383	4.22	0.09075

wc-RhB and wc-Rh6G = dyes without catalyst, $\text{SrWO}_4\text{-RhB}$ and $\text{SrWO}_4\text{-Rh6G}$ microcrystals with the dyes; $\{\}$ = absolute and $[\]$ normalized by S_{BET} .

4. Conclusions

In summary, SrWO_4 microcrystals were synthesized by the ITHAS method at 90°C for the first time. The Rietveld refinement data revealed that there are variations in the atomic positions related to the oxygen atoms, while those of strontium and tungsten atoms kept fixed into the lattice. This behavior was associated to the structural distortions on the $[\text{SrO}_8]$ and $[\text{WO}_4]$ clusters. Also, it was possible to identify a preferred crystallographic orientation in the (200) plane. The Rietveld refinement and FT-Raman spectrum proved that the SrWO_4 crystals synthesized by the ITHAS method technique are structurally ordered at long and short-range, respectively. The FE-SEM, TEM and HR-TEM images indicated that the microcrystals were formed via self-assembly of small nanocrystals, resulting in the growth of superstructures with rice-, star-, flower- and urchin-like shapes. SAED patterns confirmed that all the SrWO_4 microcrystals have monocrystal patterns. The crystal growth process occurs preferential along the [100] direction. The crystals exhibited a high PC efficiency for the degradation of Rh6G than for the RhB under UV light. Kinetic parameters suggested that the normalized $k_{[\text{Rh6G}]}$ values were 3.06 times higher than the normalized $k_{[\text{RhB}]}$ values. Finally, the PC activity of SrWO_4 microcrystals for the degradation of RhB or Rh6G dye under UV radiation was related to the defects found on the crystal surfaces as well as with the electronic structure of distorted $[\text{WO}_4]_d/[\text{SrO}_8]_d$ and ordered $[\text{WO}_4]_o/[\text{SrO}_8]_o$ clusters which play an important role in producing OH^\cdot and O_2^\cdot radicals, which are the most oxidizing species.

Acknowledgments

The authors thank the financial support of the Brazilian Research Financing Institutions: FAPESP-Postdoctorate (No. 2009/50303-4), CNPq (No. 159710/2011-1), FAPEPI-GERATEC (No. 01.08.0506.00) and CAPES.

Appendix A. Supplementary material

Supplementary data associated with this article can be found, in the online version, at <http://dx.doi.org/10.1016/j.apt.2012.08.007>.

References

- [1] G. Flor, V. Massaroti, R. Riccardi, Z. Naturforsch, Teil A 29 (1974) 503.
- [2] F. Jiandong, Z. Huanjin, W. Zhengping, G. Wenwei, W. Jiyang, Front. Chem. China. 3 (2006) 264.
- [3] F. Rivera-López, I.R. Martín, I. da Silva, C. González-Silgo, U.R. Rodríguez-Mendoza, V. Lavín, F. Lahoz, S.M. Díaz-Gozález, M.L. Martínez-Sarrion, L. Mestres, J. Fernández-Urban, High Pressure Res. 26 (2006) 355.
- [4] J.D. Fan, H.J. Zhang, J.Y. Wang, M.H. Jiang, R.I. Bougthon, D.G. Ran, S.Q. Sun, H.R. Xia, J. Appl. Phys. 100 (2006) 063513.
- [5] G. Jia, C. Tu, Z. You, J. Li, Z. Zhu, Y. Wang, B. Wu, J. Cryst. Growth 273 (2004) 220.
- [6] G. Jia, H. Wang, X. Lu, Z. You, J. Li, Z. Zhu, C. Tu, Appl. Phys. B 90 (2006) 497.
- [7] S.K. Arora, B. Chudasama, Cryst. Res. Technol. 41 (2006) 1089.
- [8] S. Wannapop, T. Thongtem, S. Thongtem, Ceram. Int. 37 (2011) 3499.
- [9] G. Tian, S. Sun, Cryst. Res. Technol. 46 (2011) 389.
- [10] T. Thongtem, S. Kungwankunakorn, B. Kuntalae, A. Phuruangrat, S. Thongtem, J. Alloys Compd. 506 (2010) 475.
- [11] L.D. Feng, X.B. Chen, C.J. Mao, Mater. Lett. 64 (2011) 2420.
- [12] Y.M. Yang, C. Liu, Y.F. Liu, B.J. Chen, H. Zhang, Chin. J. Lumin. 32 (2011) 699.
- [13] X. Zhao, T.L.Y. Cheung, X. Zhang, D.H.L. Ng, J. Yu, J. Amer. Ceram. Soc. 89 (2006) 2960.
- [14] L. Chen, Y. Gao, Mater. Res. Bull. 42 (2007) 1823.
- [15] C. Cui, J. Bi, D. Gao, J. Cryst. Growth 310 (2008) 4385.
- [16] F.Q. Dong, Q.S. Wu, D.M. Sun, Y.P. Ding, J. Mater. Sci. 43 (2008) 641.
- [17] T. Thongtem, A. Phuruangrat, S. Thongtem, Appl. Surf. Sci. 254 (2008) 7581.
- [18] J. Liao, B. Qiu, H. Wen, J. Chen, W. You, Mater. Res. Bull. 44 (2009) 1863.
- [19] T. Thongtem, S. Kaowphong, S. Thongtem, Solid State Phenom. 124 (2007) 315.
- [20] E.K. Ryu, Y.D. Huh, Mater. Lett. 62 (2008) 3081.
- [21] L. Sun, Q. Guo, X. Wu, S. Luo, W. Pan, K. Huang, J. Lu, L. Ren, M. Cao, C. Hu, J. Phys. Chem. C 111 (2007) 532.

- [22] J.C. Sczancoski, L.S. Cavalcante, M.R. Joya, J.W.M. Espinosa, P.S. Pizani, J.A. Varela, E. Longo, *J. Coll. Interf. Sci.* 330 (2009) 227.
- [23] T. Thongtem, A. Phuruangrat, S. Thongtem, *Curr. Appl. Phys.* 8 (2008) 189.
- [24] S. Liu, S. Tian, R. Xing, *CrystEngComm* 13 (2011) 7258.
- [25] H. Li, H.K. Yang, B.K. Moon, B.C. Choi, J.H. Jeong, K. Jang, H.S. Lee, S.S. Yi, *Inorg. Chem.* 50 (2011) 12522.
- [26] H. Pan, M. Hojamberdiev, G. Zhu, *J. Mater. Sci.* 45 (2012) 6083.
- [27] S. Rajagopal, D. Nataraj, O.Y. Khyzhun, Y. Djaoued, J. Robichaud, D. Mangalaraj, *J. Alloys Compd.* 493 (2010) 340.
- [28] R. Lacombe-Perales, D. Errandonea, A. Segura, J. Ruiz-Fuertes, P. Rodríguez-Hernández, S. Radescu, J. López-Solano, A. Mujica, A. Muñoz, *J. Appl. Phys.* 110 (2011) 043703.
- [29] D.W. Kim, I.S. Cho, S.S. Shin, S. Lee, T.H. Noh, D.H. Kim, H.S. Jung, K.S. Hong, *J. Solid State Chem.* 184 (2011) 2103.
- [30] L. Gracia, V.M. Longo, L.S. Cavalcante, A. Beltrán, W. Avansi, M.S. Li, V.R. Mastelaro, J.A. Varela, E. Longo, J. Andrés, *J. Appl. Phys.* 110 (2011) 043501.
- [31] E. Orhan, M. Anicete-Santos, M.A.M.A. Maurera, F.M. Pontes, C.O. Paiva-Santos, A.G. Souza, J.A. Varela, P.S. Pizani, E. Longo, *Chem. Phys.* 312 (2005) 1.
- [32] J. Yu, L. Qi, B. Cheng, X. Zhao, *J. Hazard. Mater.* 160 (2008) 621.
- [33] D. Chen, Z. Liu, S. Ouyang, J. Ye, *J. Phys. Chem. C* 115 (2011) 15778.
- [34] Z. Shan, Y. Wang, H. Ding, F. Huang, *J. Mol. Catal. A* 302 (2009) 54.
- [35] S. Brunauer, P.H. Emmett, E. Teller, *J. Amer. Chem. Soc.* 60 (1938) 309.
- [36] G. Jia, C. Wang, S. Xu, *J. Phys. Chem. C* 114 (2010) 17905.
- [37] D. Errandonea, J. Pellicer-Porres, F.J. Manjón, A. Segura, Ch. Ferrer-Roca, R.S. Kumar, O. Tschauner, P. Rodríguez-Hernández, J. López-Solano, S. Radescu, A. Mujica, A. Muñoz, G. Aquilanti, *Phys. Rev. B* 72 (2005) 174106.
- [38] P. Rodríguez-Hernández, J. López-Solano, S. Radescu, A. Mujica, A. Muñoz, D. Errandonea, J. Pellicer-Porres, A. Segura, Ch. Ferrer-Roca, F.J. Manjón, R.S. Kumar, O. Tschauner, G. Aquilanti, *J. Phys. Chem. Solids* 67 (2006) 2164.
- [39] H.M. Rietveld, *Acta Crystallogr.* 22 (1967) 151.
- [40] <http://www.ing.unitn.it/~maud/>.
- [41] M. Ferrari, L. Lutterotti, *J. Appl. Phys.* 76 (1994) 7246.
- [42] K. Momma, F. Izumi, *J. Appl. Crystallogr.* 44 (2011) 1272.
- [43] A. Wang, C. Wang, G. Jia, *Front. Chem. Chin.* 5 (2010) 61.
- [44] V.M. Longo, E. Orhan, L.S. Cavalcante, S.L. Porto, J.W.M. Espinosa, J.A. Valera, E. Longo, *Chem. Phys.* 334 (2007) 180.
- [45] L.S. Cavalcante, V.M. Longo, J.C. Sczancoski, M.A.P. Almeida, A.A. Batista, J.A. Varela, M.O. Orlandi, E. Longo, M.S. Li, *CrystEngComm* 14 (2012) 853.
- [46] Z.C. Ling, H.R. Xia, D.G. Ran, F.Q. Liu, S.Q. Sun, J.D. Fan, H.J. Zhang, J.Y. Wang, L.L. Yu, *Chem. Phys. Lett.* 426 (2006) 85.
- [47] T.T. Basiev, A.A. Sobol, Y.K. Voronko, P.G. Zverev, *Opt. Mater.* 15 (2000) 205.
- [48] A. Golubovic, R. Gajic, Z. Dohcevic-Mitrovic, S. Nikolic, *J. Alloys Compd.* 415 (2006) 16.
- [49] K.P.F. Siqueira, R.L. Moreira, M. Valadares, A. Dias, *J. Mater. Sci.* 45 (2009) 6083.
- [50] J.C. Sczancoski, M.D.R. Bomio, L.S. Cavalcante, M.R. Joya, P.S. Pizani, J.A. Varela, E. Longo, M.S. Li, J.A. Andrés, *J. Phys. Chem. C* 113 (2009) 5812.
- [51] S.P.S. Porto, J.F. Scott, *Phys. Rev.* 157 (1967) 716.
- [52] T. Thongtem, A. Phuruangrat, S. Thongtem, *J. Nanopart. Res.* 12 (2010) 2287.
- [53] S. Degreniers, S. Jandl, C. Carlone, *J. Phys. Chem. Solids* 45 (1984) 1105.
- [54] T. Thongtem, A. Phuruangrat, S. Thongtem, *J. Ceram. Proces. Res.* 9 (2008) 258.
- [55] L.S. Cavalcante, J.C. Sczancoski, R.L. Tranquilin, J.A. Varela, E. Longo, M.O. Orlandi, *Particuology* 7 (2009) 353.
- [56] Y. Zhao, C. Li, X. Liu, F. Gu, *J. Alloys Compd.* 440 (2007) 281.
- [57] T. Wu, G. Liu, J. Zhao, H. Hidaka, N. Serpone, *J. Phys. Chem. B* 102 (1998) 5845.
- [58] J. Bi, L. Wu, Y. Zhang, Z. Li, J. Li, X. Fu, *Appl. Catal. B* 91 (2009) 135.
- [59] G.J. Xing, R. Liu, C. Zhao, Y.L. Li, Y. Wang, G.M. Wu, *Ceram. Int.* 37 (2011) 2951.
- [60] L. Zhen, W.S. Wang, C.Y. Xu, W.Z. Shao, M.M. Ye, Z.L. Chen, *Script. Mater.* 58 (2008) 461.
- [61] H. Fu, C. Pan, L. Zhang, Y. Zhu, *Mater. Res. Bull.* 42 (2007) 696.
- [62] D. Ye, D. Li, W. Zhang, M. Sun, Y. Hu, Y. Zhang, X. Fu, *J. Phys. Chem. C* 112 (2008) 17351.
- [63] A. Zhang, J. Zhang, *J. Mater. Sci.* 45 (2010) 4040.
- [64] A.R. Malagutti, H.A.J.L. Mourão, J.R. Garbin, C. Ribeiro, *Appl. Catal. B* 205 (2009) 205.
- [65] J. Bi, L. Wu, Z. Li, Z. Ding, X. Wang, X. Fu, *J. Alloys Compd.* 480 (2009) 684.
- [66] T. Saison, N. Chemin, C. Chanéac, O. Durupthy, V. Ruau, L. Mariey, F. Maugé, P. Beaunier, J.P. Jolivet, *J. Phys. Chem. C* 115 (2011) 5657.
- [67] L.S. Cavalcante, F.M.C. Batista, M.A.P. Almeida, A.C. Rabelo, I.C. Nogueira, N.C. Batista, J.A. Varela, M.R.M.C. Santos, E. Longo, M.S. Li, *RSC Adv.* 2 (2012) 6438.